GEOPERSIA

Accepted Manuscript

Limestone Strength Prediction: A Data-Driven Machine Learning Framework in Dry and Saturated Conditions

Mehrdad Amiri, Gholam Reza Lashkaripour, Naser Hafezi Moghaddas, Mohammad Hossein Ghobadi, Mojtaba Amiri, Danial Jahed Armaghani, Luís Sousa

DOI: 10.22059/geope.2026.412083.648869

Receive Date: 27 February 2026
Revise Date: 01 August 2026
Accept Date: 08 August 2026

Limestone Strength Prediction: A Data-Driven Machine Learning Framework in Dry and Saturated Conditions

Mehrdad Amiri [1], *, Gholam Reza Lashkaripou [1], Naser Hafezi Moghaddas [1], Mohammad Hossein Ghobadi [2], Mojtaba Amiri [3], Danial Jahed Armaghani [4], Luís Sousa [5]

[1] Department of Geology, Faculty of Science, Ferdowsi University of Mashhad, Mashhad, Iran
[2] Department of Geology, Faculty of Science, Bu-Ali Sina University, Hamedan, Iran
[3] School of Electrical and Computer Engineering, College of Engineering, University of Tehran, Tehran, Iran
[4] School of Civil, Environmental & Sociotechnical Engineering, University of Technology Sydney, Ultimo, NSW 2007, Australia
[5] Department of Geology, University of Trás-os-Montes and Alto Douro, Vila Real, Portugal - CGeo Research Centre, University of Coimbra, Coimbra, Portugal

Received: 27 February 2026, Revised: 01 August 2026, Accepted: 08 August 2026

Abstract
The uniaxial compressive strength (UCS) is a critical property in rock mechanics, widely used in mining, drilling, tunneling, slope stability assessment, and geotechnical design. It is a fundamental indicator of the load-bearing capacity and failure behavior of rock materials and plays a central role in engineering decision-making. Direct UCS testing, however, is costly, time-consuming, and often impractical, especially for weak, weathered, or fractured rocks where obtaining intact core samples is difficult. Laboratory preparation, standardization requirements, and equipment limitations further restrict extensive testing programs. For these reasons, reliable predictive models based on easily measurable physical and mechanical properties are highly valuable. While various predictive models exist, few studies apply ensemble machine learning (ML) approaches under both dry and saturated conditions, particularly for region-specific formations. Moisture conditions significantly influence the mechanical response of carbonate rocks, yet this factor is frequently neglected in predictive modeling. This study investigates UCS prediction from the Ilam formation in southwest Iran using physical and mechanical properties collected from limestone samples tested in both dry and saturated states. Four models random forest (RF), deep neural network (DNN), AdaBoost, and multivariate regression (MR) were evaluated using K-fold cross-validation to ensure robust and unbiased performance assessment. Model performance was assessed via the mean square error (MSE) and coefficient of determination metrics. Results show that all models provide accurate predictions, with RF and DNN performing best under dry and saturated conditions, respectively. The study introduces a novel comparative framework and dataset for UCS prediction in Ilam limestone, supporting more efficient, reliable, and data-driven geotechnical assessments.

Keywords: Uniaxial Compressive Strength (UCS), Machine Learning (ML), Deep Neural Network (DNN), Random Forest (RF), Adaboost, Multivariate Regression (MR).

Introduction

The uniaxial compressive strength (UCS) parameter of rocks is a vital property of rock in engineering projects, for example foundations, tunnel buildings, slopes, rock excavations,

---

* Corresponding author e-mail: a.mehrdad1372@yahoo.com

stability analyses, underground mining applications, etc. The UCS is a key factor in the design of rock engineering structures and is essential for the classification of rock masses. This characteristic has a crucial impact on the design and implementation of mining activities, including the stability of mine wall slopes, trench design, and drilling and blasting operations (Hoek & Diederichs, 2006; Shen et al., 2012). Nevertheless, to determine this parameter, complicated equipment, high-quality core specimens and time-consuming procedures are required. It is important to highlight obtaining a suitable core from weak, crushed, and crushed rocks is a significant problem (Fener et al., 2005). For this reason, in the implementation stages of a geotechnical project, indirect methods are employed to estimate the UCS parameter (Gül et al., 2021; Yesiloglu-Gultekin & Gokceoglu, 2022).Many researchers have predicted the UCS parameters of different types of rocks using experimental relationships via simple and multiple regression analysis, as well as the development of different models of neural networks (e.g., Heidari et al., 2012; Kumar et al., 2013; Ozcelik et al., 2013; Nefeslioglu, 2013; Madhubabu et al., 2016; Moussas & Diamantis, 2021; Yesiloglu-Gultekin & Gokceoglu, 2022). For example, an artificial neural network (ANN) model have been developed to predict UCS in soluble and shear rocks (Yilmaz & Yuksek, 2009; Kahraman et al., 2009) , and fracture durability effects on UCS of carbonate rocks have been evaluated (Yagiz et al., 2012). They showed that the accuracy of the ANN is much greater than that of other methods. Torabi-Kaveh et al., (2015) applied ANN and regression models to estimate the UCS of Asmari limestone using physical properties. Other studies have employed non-destructive tests such as unit weight, Schmidt hammer, and ultrasonic velocity for UCS prediction (Li et al., 2020; Kayabasi et al., 2003). In Table 1, more prediction models are summarized.

With the advancement of computing hardware, machine learning (ML) methods are increasingly applied to data and signal prediction tasks in geotechnical engineering and rock mechanics (e.g., Sonmez et al., 2006; Yagiz et al., 2012; Mishra & Basu, 2013; Mohamad et al., 2015; Mozumder & Laskar, 2015; Armaghani et al., 2016; Madhubabu et al., 2016; Ferentinou & Fakir, 2017; Sharma et al., 2017; Jahed Armaghani et al., 2018; Tang & Na, 2021; Yesiloglu-Gultekin & Gokceoglu, 2022).

Despite these developments, there remains a notable gap in the literature concerning the use of ensemble learning frameworks that comparatively evaluate multiple ML models on site-specific datasets. Additionally, prior studies rarely consider both dry and saturated states of limestone samples. This study addresses these gaps by proposing a comparative ensemble-based machine learning approach for predicting UCS, incorporating both dry and saturated conditions and targeting the Ilam formation limestones in southwest Iran-a formation with strategic importance for oil and gas exploration. The objective of this study is to estimate the UCS of the Ilam limestone formation in SW Iran using physical and mechanical parameters indirectly using statistical and learning methods. The Ilam limestone formation is very important in oil and gas projects. In this study, Random Forest (RF), Deep Neural Networks (DNN), AdaBoost, and multivariate regression (MR) models are employed. The choice of RF and AdaBoost is motivated by their robustness in handling nonlinear relationships and noise-prone datasets, while DNN is selected for its capacity to model complex patterns and interactions among features. These models are compared to highlight performance strengths and limitations under varying conditions. Unlike other previously models, the selected algorithms offer a balance of interpretability, accuracy, and computational efficiency suitable for this domain. The significant outcomes of this study can be summarized as:

Development of a comparative machine learning framework for systematic evaluation and prediction of UCS under both dry and saturated conditions.

Simultaneous incorporation of both dry and saturated limestone conditions into the machine-learning modeling framework to enhance prediction robustness across varying moisture states.

Application of the proposed machine-learning models to the Ilam Limestone formation, a geologically and economically important unit in southwestern Iran, providing a case-specific framework for reliable UCS prediction.

Development of a new empirical equation for predicting uniaxial compressive strength (UCS) based on experimentally measured limestone properties.

Justification and evaluation of multiple ML approaches, including RF, DNN, and AdaBoost, alongside traditional MR.

Experimental characterization of the physical and mechanical properties of the Ilam formation, generating a comprehensive dataset for UCS prediction and machine-learning model development.

Table 1. Some previous studies to predict the UCS

References	Predictive Model	Input
(Kahraman, 2001)	Simple regression analysis	Is_{50}, Rn, Vp, impact strength
(Gokceoglu, 2002)	FIS	Petrographical compositions
(Zorlu et al., 2008)	Multiple regression analysis, ANN	Quartz content, PD, GC
(Çanakcı et al., 2009)	Gene expression programming, ANN	Iv, n, Rn, Vp, γ_d
(Cevik et al., 2011)	ANN	I_d, clay content
(Monjezi et al., 2012)	Multiple regression analysis, neuro-genetic approach	n, γ, Rn
(Ozbek et al., 2013)	GEP	n, w, γ
(Yesiloglu-Gultekin et al., 2013)	Simple and multiple regression analysis, ANFIS	quartz, orthoclase and plagioclase contents
(Armaghani et al., 2016)	Regression analysis, ANN	SH, Vp, Is_{50}
(Teymen & Mengüç, 2020)	Simple and multiple regression analysis, ANN, ANFIS and genetic expression programming	γ, Is_{50}, BTS, SH, Rn, Vp
(Barham et al., 2020)	ANN	SH, Vp, Is_{50}, BTS, γ, SDI
(Wang et al., 2020)	RF	SH, Vp
(Armaghani et al., 2021)	ANN	n, Vp
(Fang et al., 2021)	ANN, hybrid ANN with imperialism competitive algorithm (ICA–ANN), hybrid ANN with artificial bee colony (ABC–ANN) and genetic programming (GP)	n, Is_{50}, Rn, Vp
(Gül et al., 2021)	Multilayer Perceptron Neural Network (MLPNN), M5 Model Tree (M5MT), Extreme Learning Machine (ELM)	BTS, Vp, SH
(Moussas & Diamantis, 2021)	Regression analysis, ANN	n, Is_{50}, SH, Vp, Ser (%)
(Diamantis & Moussas, 2021)	Regression analysis, ANN	γ_s, γ_d, n, Is_{50}, SH, Vp
(Jin et al., 2022)	GWO-ELM	SH, Vp, Is_{50}, n

(Zhao et al., 2022)	GPR	SH, Vp, Is_{50}, n
(Li et al., 2022)	TSO- RF	SH, Vp, Is_{50}, n, γ
(Zhao et al., 2023)	DFNN	Drilling jumbo measurement data
(Abdelhedi et al., 2023)	XGB	Vp, n, γ
(Yu et al., 2023)	Regression analysis, ANN, MPA	Is_{50}, RL, Vp
(Wang et al., 2023)	PSO-RF	SH, Vp, Is_{50}, γ
(Asteris et al., 2024)	ANN models	n, Vp, SH
(Amiri et al., 2024)	DNN, PCA	γ, Iv, Is_{50}, Vp, BTS
(Setayeshirad et al., 2025)	Regression analysis, ANN	n, γ, Iv, Vp, Vs, BTS
(Lawal and Mulenga., 2025)	ANN, GPR	n, Vp, $Is_{50,}$ SH

Geological setting and stratigraphy

The platform of the Arabian and Zagros fold-thrust belt were placed at tropical and subtropical latitudes throughout the Late Cretaceous. The Cretaceous successions in this area include thick sedimentary packages (e.g., Ghabeishavi et al., 2009; Hollis, 2011). In paleogeographical research on the Cretaceous, a ramp-type depositional structure related to paleogeographical research conducted on Cretaceous formations, a ramp-type depositional structure related to shelf carbonates is proposed, which gradually surrounded a large proportion of the Middle East area in response to eustatic sea-level rise (Alavi, 2004; Heydari, 2008; Navidtalab et al., 2020). Throughout the Zagros Basin, the combined effects of tectonic events and sea level fluctuations make the platforms of carbonate and the formation of karstified distances and paleosols, especially in the Cenomanian-Turonian intervals of the Ilam formation. The occurrence of several paleohighs and troughs has been documented, which exerted influence on the characteristics of facies, variations in thickness, diagenetic history, and reservoir quality (Mehrabi et al., 2015; Navidtalab et al., 2020). The upper Ilam and Sarvak formations (Cenomanian–Campanian) are characterized by dominant (argillaceous/dolomitic) limestone as shown in Fig. 1 (Motiei, 1993). These reservoirs are referred to as the Bangestan group, recognized as the second most important oil reservoirs in the Zagros region, following the Oligocene–Miocene Asmari formation (Al-Husseini, 2007; Motiei, 1993). The Ilam formation-type section is located in Tange Gorab of the Ilam Province. This area is between Surgah Mountain (southwest side) and Kabirkoh (northwest side). The upper and lower formation of the type section in this area are the Surgah and Gurpi formations, respectively. It is important to highlight that the type section coordinates of the Ilam formation are N: 33° 35′ 09″ and E: 46° 19′ 06″. The Ilam formation is primarily composed of shallow marine limestones and is succeeded conformably by the marl and shale sequences of the Gurpi formation. In contrast, it rests unconformably above the carbonate strata of the Sarvak formation, reflecting a distinct geological boundaryThe Ilam formation has several stratigraphic counterparts across the Middle East, including the Halul formation in Oman, the Fiqa formation in the United Arab Emirates, and the Aruma formation in Qatar. Moreover, equivalent units such as the Gudair formation in Saudi Arabia and the Kometan-Shiranish formations in eastern Iraq highlight the regional geological continuity. 60 block samples were collected and transferred from Ilam formation in southwestern of Iran. These block samples vary from $30 \times 40 \times 40$ cm^3 to $40 \times 50 \times 50$ cm^3. In Fig. 2, the location of sampling is shown. As can be seen, the type, name, and location of these samples are shown.

Material and methods

Petrographical properties

The mineralogy and texture of the studied rocks were performed. In addition, the samples were named based on the classifications of Dunham (1962). It is noteworthy that, thin sections are the basis of existing classifications for limestone. In this study, thin sections were prepared from all lithological changes in the Ilam limestone formation. In this study, the Ilam limestone formation is grouped into three classes. The names of the limestone sections are determined based on the standard of Dunham (1962). Table 2 and Fig.3 show selected photomicrographs of the limestone sections of the Ilam formation. Generally, microfacies include bioclast wackestone, bioclast wackestone – packstone, bioclast packstone textures that indicate deposition under low to medium-energy conditions in open marine settings.

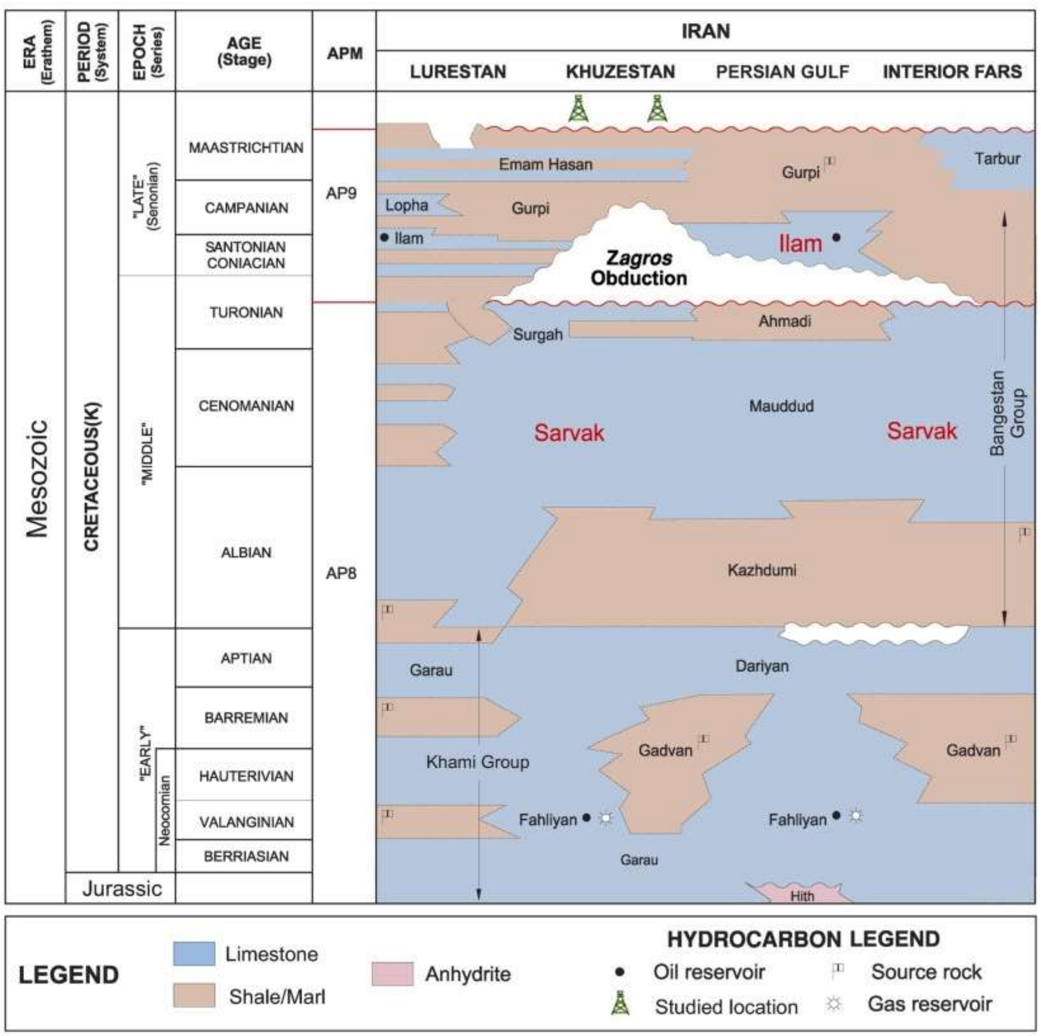

Figure1. Stratigraphy of the Cretaceous successions in various regions of the Zagros (Mehrabi et al., 2020)

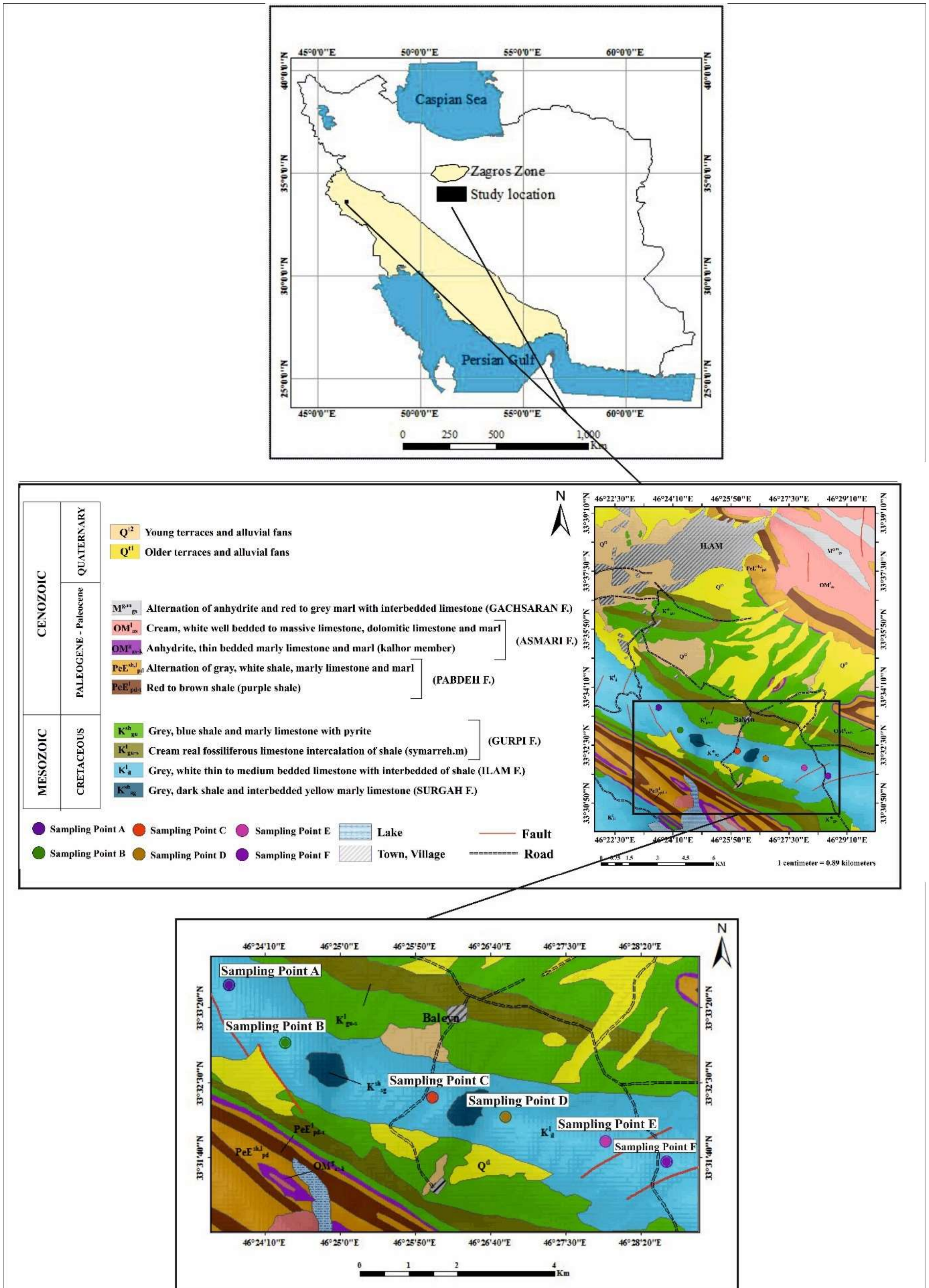

Figure 2. Location map of the study area showing the geological setting and sampling sites

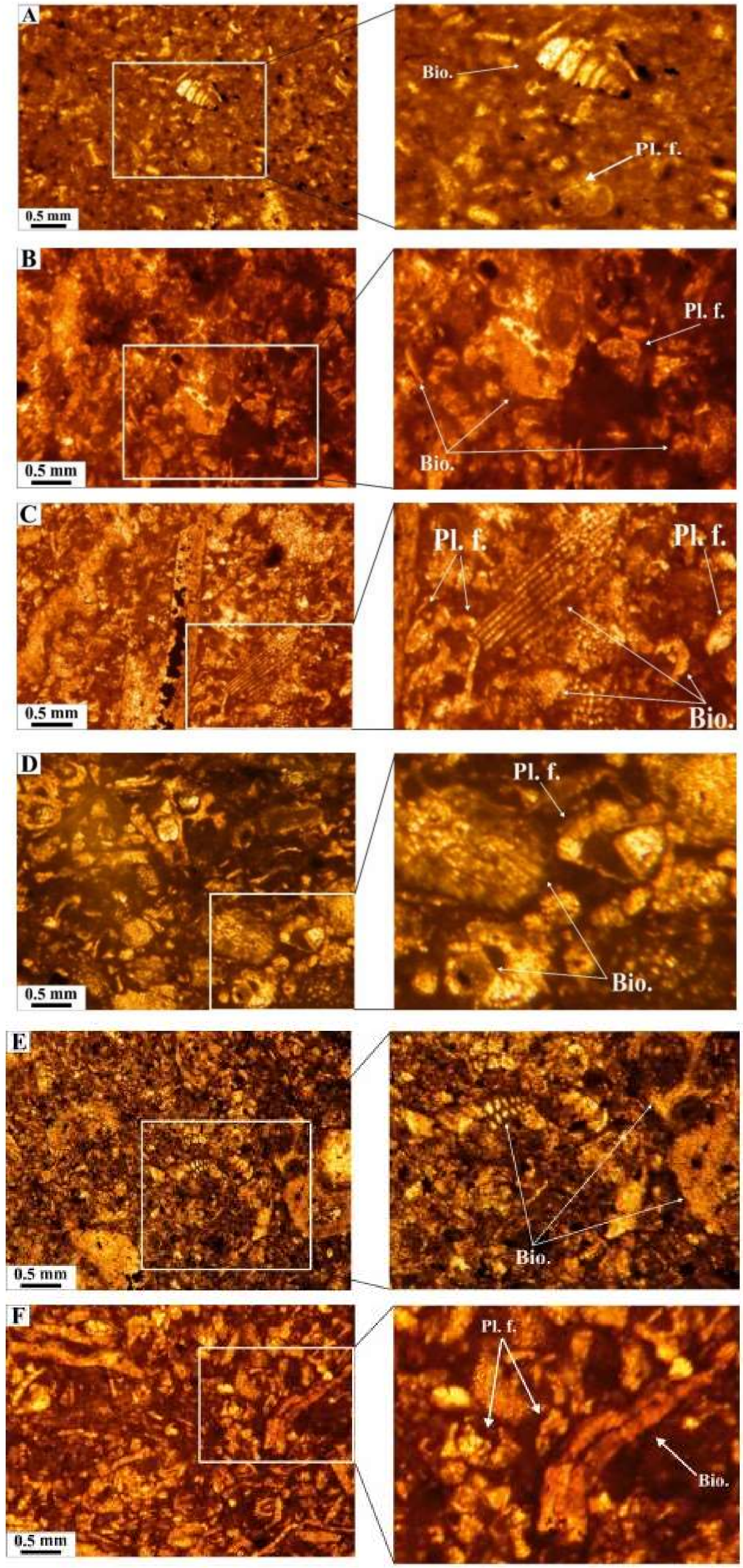

Figure 3. Representative photomicrographs of the Ilam formation in the type section A, B, C, D, E, and F. Abbreviations: Pl. f: Planktonic foraminifera, Bio: Bioclast. for more details refer to Table 2

Table 2 Microfacies of the Ilam formation in the type section

Code	Name & Allochems	Setting	porosity	Energy
A	■ Planktonic foraminifera Bioclast Wackestone ■ Pl. f: Planktonic foraminifera, Bio: Bioclast	Open marine	intragranular	Low
B	■ Planktonic foraminifera Bioclast Wackestone ■ Pl. f: Planktonic foraminifera, Bio: Bioclast	Open marine	Intergranular & intragranular	Low
C	■Bioclast Planktonic foraminifera Wackestone-packstone ■ Pl. f: Planktonic foraminifera, Bio: Bioclast	Open marine	Intergranular & intragranular	Low-Medium
D	■ Planktonic foraminifera Bioclast Wackestone-packstone ■ Pl. f: Planktonic foraminifera, Bio: Bioclast	Open marine	Intergranular & intragranular	Low-Medium
E	■ Bioclast packstone ■ Small foraminifera with a porcelaneous shell	Open marine	Intergranular & intragranular	Medium
F	■ Bioclast Planktonic foraminifera packstone ■ Pl. f: Planktonic foraminifera, Bio: Bioclast	Open marine	intragranular	Medium

Preparing Samples

In the laboratory, rock blocks were cored with diamond coring bits (vertical direction) having a diameter of 54.7 mm. The ends of the specimens were then flattened and precisely aligned perpendicular to their axes using a polishing and lapping machine. A macroscopic inspection was conducted on the specimens, and only those exhibiting homogeneity, isotropy, no weathering, and no visible joints, fissures, cracks, or other discontinuities were selected for use.

Physical Properties

The evaluation of the physical characteristics of rock is serious in engineering geology, mining, and civil projects. These characteristics rely on the microcracks and mineral content of the intact rock. Microcracks including cleavage plane and grain boundaries, which rock strength decreased with an increase in them. In addition, mineral contents including feldspar, calcite, quartz, muscovite, biotite and clay minerals, which have influenced by the type, percentage, composition of minerals, and texture (Willard & McWilliams, 1969; Shalabi et al., 2007).

Water absorption (I_v (%)), unit weight (γ) under dry and saturated conditions, and porosity (n (%)) are the major features that control the other features of rock, such as the ultrasonic P-wave velocity (V_p), ultrasonic S-wave velocity (V_s), Brazilian tensile strength (BTS), UCS, and point load index (Is50). The water absorption, unit weight, and porosity were characterized by the buoyancy method according to ISRM (2007). The results of these characterizations are given in Table 3.

Table 3. Statistics of the variables

Parameters	Min	Max	Mean	Std. E	Std. D	Kurtosis	Skewness
γ_{sat} (kN/m^3)	21.765	27.980	26.201	0.150	1.154	8.842	-2.181
γ_d (kN/m^3)	21.678	27.835	26.070	0.148	1.142	8.793	-2.159
n (%)	0.581	2.225	1.276	0.058	0.449	1.978	0.288
Iv (%)	0.212	1.050	0.485	0.024	0.189	3.709	0.929
UCS $_{dry}$ (MPa)	70.134	143.733	99.245	2.074	15.931	3.196	0.556
UCS $_{sat}$ (MPa)	46.066	98.901	67.257	1.494	11.475	3.056	0.484
BTS $_{dry}$ (MPa)	6.361	15.869	10.249	0.332	2.553	1.998	0.203
BTS $_{sat}$ (MPa)	4.117	9.980	7.022	0.203	1.565	2.376	-0.218
Is$_{50\ dry}$ (MPa)	2.547	7.012	4.851	0.126	0.967	2.951	-0.096
Is$_{50\ sat}$ (MPa)	1.840	5.538	3.402	0.132	1.018	2.251	0.394
Vp $_{dry}$ (m/s)	1251.564	7708.333	3685.826	218.281	1676.655	2.177	0.355
Vp $_{sat}$ (m/s)	1895.307	9433.962	5281.32	279.911	2150.039	2.197	0.152
Vs $_{dry}$(m/s)	826.032	5087.50	2432.645	144.066	1106.592	2.177	0.355
Vs $_{sat}$(m/s)	1250.903	6226.415	3485.671	184.741	1419.026	2.197	0.152

Dynamic and mechanical properties

The UCS is analyzed as a crucial factor in addressing engineering challenges such as ground stability, excavation planning, and infrastructure development (Singh et al., 2013). The UCS was determined by the ISRM (2007). The UCS tests were applied on 54.7mm core samples with a length to diameter ratio of 2.5. The loading was applied in that way so that the sample should be failed between 5 and 15 minutes. The loading rate between 0.5 and 1 MPa per second was applied. Each sample underwent ten test repetitions, and the average of these results was recorded as the UCS. It is important to highlight that the maximum load at failure was applied to calculate the UCS of the specimens.

The point load index (Is50) has been regarded as a suitable testing approach for estimating rock strength, owing to its straightforward testing process, and simplicity in specimen preparation. It has been described as an indirect measure of the compressive or tensile strength of rocks(Fereidooni and Khajevand et al, 2018). The experiment was conducted on cylindrical core specimens measuring 54.7 mm in diameter, with a length-to-diameter ratio of approximately 1.2. It is important to highlight that this test has done by the axial method. In this test, loading was applied on core samples with a rate of 0.1 kN/S. The methods suggested under the ISRM (2007).

The BTS test, fundamental and straightforward geomechanical assessment, was employed in this research. Testing was conducted on core samples measuring 54.7 mm in diameter, maintaining a thickness-to-diameter ratio of 0.5. The procedure adhered to the ISRM (2007) with a loading rate applied at 0.2 kN/s during the test.

The ultrasonic P-wave velocity (V_p) and ultrasonic S-wave velocity (V_s) (nondestructive tests) were characterized on the cylindrical shape core specimens under the ASTM D 2845-05 (2005). It is important to highlight that the ends of the specimens of core rock are formed flat and vertical to the axis of the specimens. Also, all sides are smoothed by polishing and lapping machine. In the following, the end of core samples is covered with stiffer grease to provide a good coupling and maximize the accuracy of the transit time measurement. The ultrasonic P-wave velocity (V_p) and ultrasonic S-wave velocity (V_s) test carried out on 54.7mm core samples with a length to diameter ratio of 2.5. Also, to determine the parameters using a Pundit testing machine, the pulse generation method is used as Fig. 4. The results of these characterizations are given in Table 3. Furthermore, the definition of required parameters are defined in Table 4.

Dataset

In this article, 60 block samples are used for statistical analysis, and six specimens are obtained from each block sample (three samples for dry condition and three samples for saturated condition). Subsequently, the mean value of the three specimens of each block sample for dry and saturated conditions was recorded. Table 3 displays the outcomes of these evaluations, providing a statistical overview of the physical and mechanical characteristics contained within the dataset. Based on the classification of Broch and Franklin (1972), the strength of these rocks is variated from high to very high and according to the ISRM (2007), the strength of these rocks is variated from very low to high. According to Anon (1979) classification, the porosity of these rocks is classified from very low to low. According to Anon (1979) classification, the unit weight of these rocks is classified from low to very high. The correlation matrix of data for dry and saturated conditions are presented in Fig 5. (a) and (b) based on equation 1.

$$C_{xy} = \frac{\sum_{i=1}^{n}(x_i-\frac{1}{n}\sum_{i=1}^{n}x_i)(y_i-\frac{1}{n}\sum_{i=1}^{n}y_i)}{\sqrt{\sum_{i=1}^{n}\left(x_i-\frac{1}{n}\sum_{i=1}^{n}x_i\right)^2}\sqrt{\sum_{i=1}^{n}\left(y_i-\frac{1}{n}\sum_{i=1}^{n}y_i\right)^2} \quad (1)$$

where x_i and y_i are a pair samples of properties. n is the number of samples.

Table 4. Definition of the parameters.

Parameter	Description	unit
V_t	The total volume of the specimen	m^3
W_d	The dry weight of the specimen	kN
W_{sat}	The saturated weight of the specimen	kN
F	The failure load	N
A	The area of the cylindrical specimen	mm^2
D_e	The equivalent core diameter	mm
P	Peak load	kN
W	The smallest specimen width perpendicular to the loading direction	mm
D	The distance between the platens at failure	mm
T	The thickness of the disc	mm
d	The diameter of the disc	mm
t	The pulse travel time	s
L	The length of specimen	m

Figure 4. Experimental set up in laboratory with samples

According to this Figure, the highest Pearson correlation is between point load and Brazilian test strength and its value is equal 0.85 and 0.74 for dry and saturated conditions, respectively. The correlations between Brazilian test and water absorption and porosity are 0.67 and 0.69, respectively, under dry conditions. Because water absorption expresses the empty space in the rock for water absorption and the type of minerals and rock matrix. The features of the datasets that is used in this study are shown in Fig. 6.

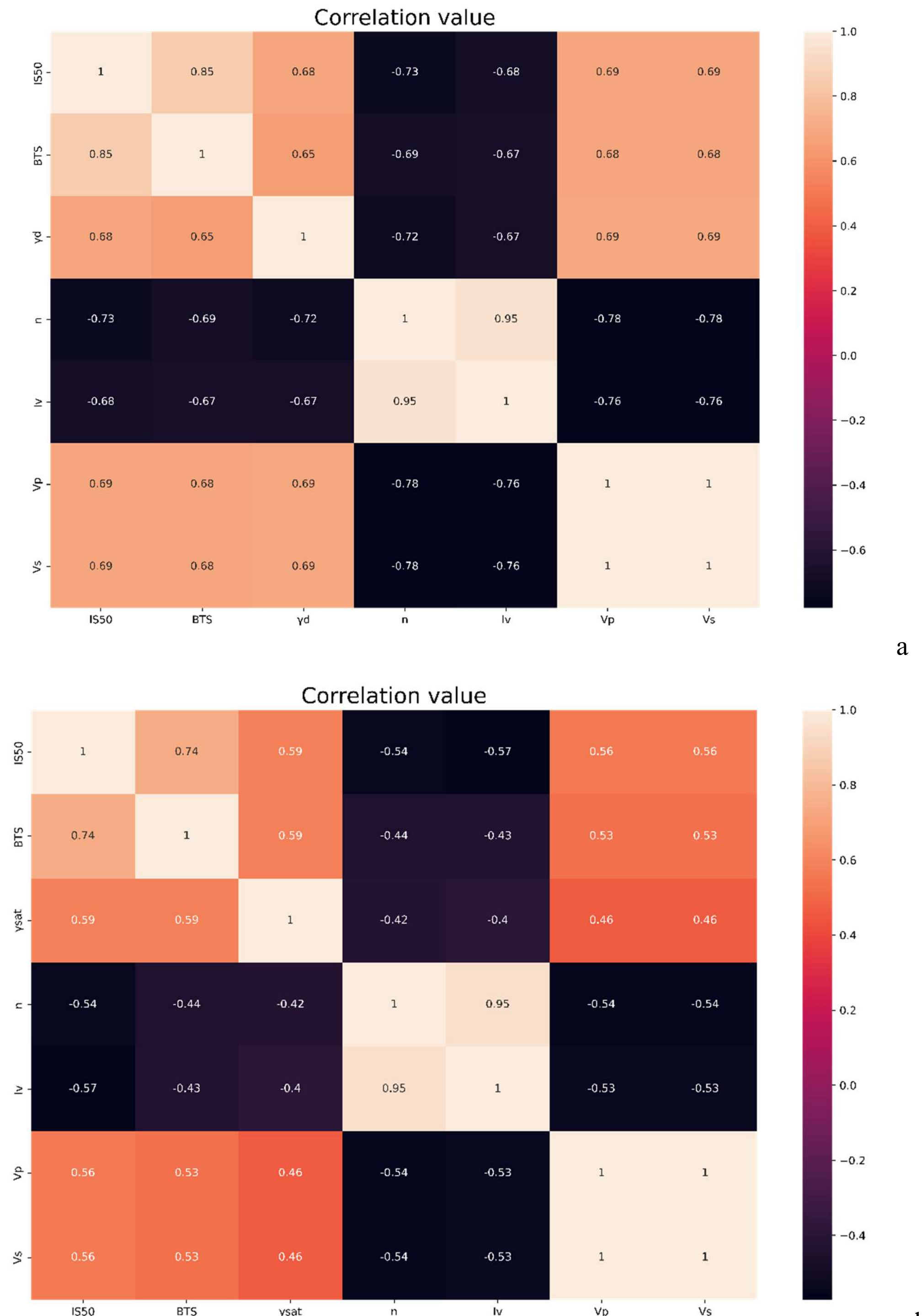

Figure 5. The correlation coefficient of all input data a) Dry condition b) Sat condition

Uniaxial compressive strength (UCS) prediction

In this section, different methods are proposed to predict the UCS. These methods have been described previously (Fausett, 2006; Russell, 2010; Flasiński, 2016; Zhang et al., 2021). The flowchart of the prediction model is illustrated in Fig. 7. There are five main steps to implement this aim: a) preprocessing the data, b) splitting the prepared dataset, c) selecting a model, d) applying the K-fold method and using the average as the score, and e) reporting the result.

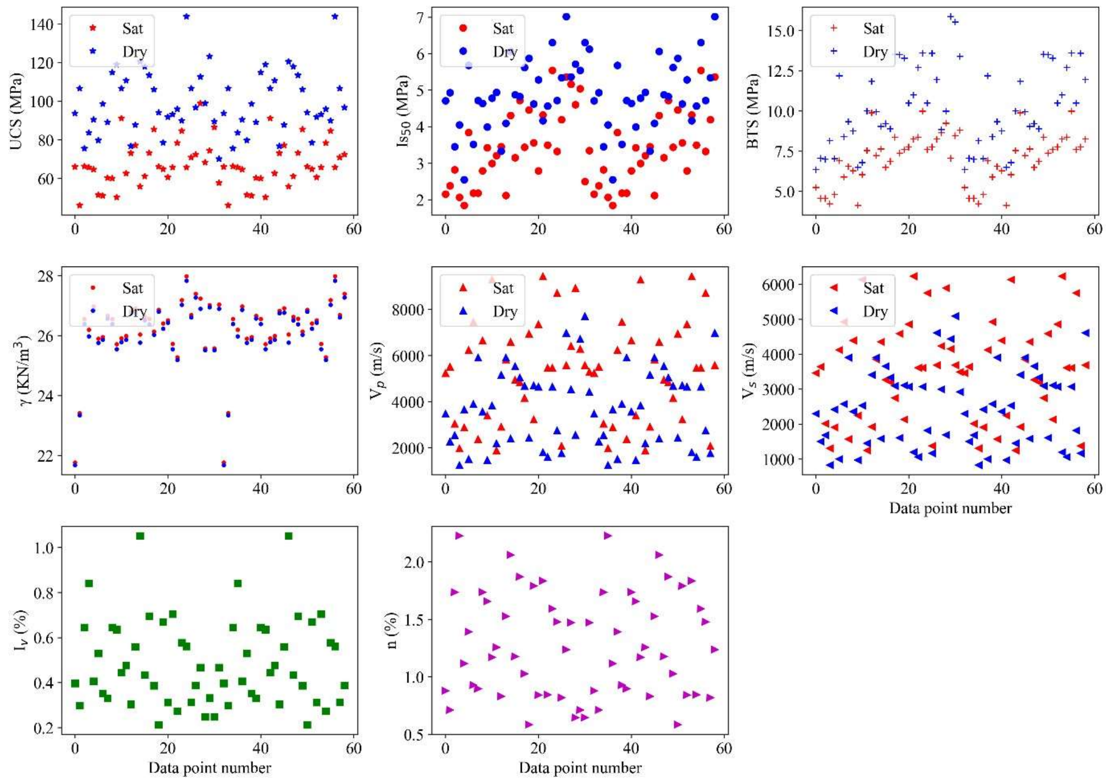

Figure 6. Different features of dataset

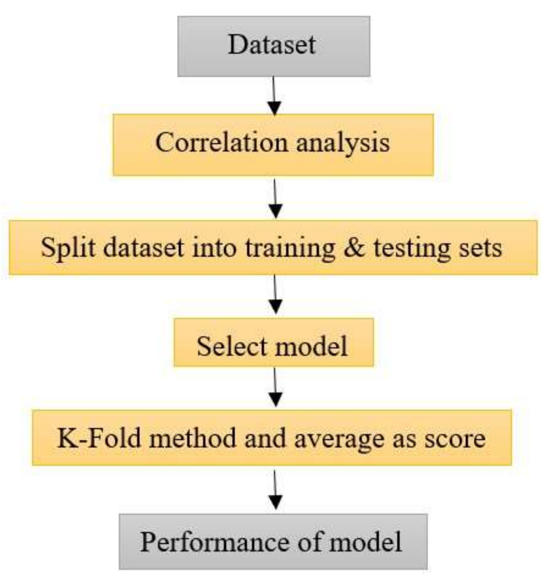

Figure 7. Flowchart of the prediction models

Preprocessing data

Data preprocessing is used to increase performance and is an important process in the preprocessing of data. This stage includes cleaning and removing outliers, data reduction, normalization, etc. In this study, each column scales and translates individually such that it is within the given range of the set, i.e., between zero and one (Haykin & Haykin, 2001).

$$x_{new} = \frac{x - x_{min}}{x_{max} - x_{min}} \quad (2)$$

where x_{min} and x_{max} are the minimum and the maximum values for each column of the dataset, respectively. In the following, bold uppercase letters denote matrices, whereas bold lowercase letters represent vectors. Furthermore, $(.)^T$ denotes the transpose operator, and $\|.\|_2$ represents the Euclidean norm of a vector.

Multivariate regression (MR)

The multivariate regression (MR) method is a supervised method involving multiple data variables. The MR is a statistical technique used to model the relationship between one dependent variable and several independent variables. It helps predict the dependent variable and assess how it varies in response to changes in the independent variables. The MR equation is as follows:

$$y = c + g_1 x_1 + g_2 x_2 + \cdots + g_D x_D \quad (3)$$

where c and g_i are the constant and the ith regression coefficients, respectively. In addition, y is the dependent variable, and $x_1, \ldots, x_D$ are independent variables (Duda and Hart , 2006). The constant parameter can be transformed into a set of coefficients whose value of x_0 is equal to one. Therefore, equation (3) in matrix form can be written as

$$y = gx^T \quad (4)$$

where $g = [c, g_1, \ldots, g_D]$ and $\mathbf{x} = [1, x_1, \ldots, x_D]$. In this study, the dependent variable is the UCS parameter, and γ, n, V_p and Is_{50} are independent variables.

Artificial neural network (ANN)

An ANN that contains neurons is a supervised learning method of ML. These neurons connect to each other in various ways and create a network. An ANN includes input, hidden, and output layers. The number of neurons within each layer, number of hidden layers, the activation function (AF), batch size, optimizer, and the number of epochs are vital parameters for the DNN. In this work, a multilayer perceptron (MLP) is used to predict the UCS. The MLP method is a feed-forward network that includes an arbitrary number of fully/partially connected layers with an arbitrary number of neurons. The simple NN (SNN) model has a single layer, but the DNN involves I linear combinations of the input's statistical variables, $x_1, \ldots, x_D$, in the following form:

$$a_i = \sum_{f=1}^{D} g_{if} x_f + b_i, \ i = 1, \ldots, I \quad (5)$$

where g_{if} and b_i are weight and bias, respectively. Also, this model is written as

$$a_i = \sum_{f=0}^{D} g_{if} x_f, \ i = 1, \ldots, I \quad (6)$$

It is noteworthy that $x_0 = 1$ and $g_{i0} = b_i$. Thus, output of the ith neuron on a layer of the SNN model is

$$z_i = AF(a_i), \ i = 1, \ldots, I \quad (7)$$

where I and AF(.) are the total number of neurons and a proper activation function, respectively. The weight as form of matrix can be written as

$$G = \begin{bmatrix} g_{10} & \cdots & g_{1D} \\ \vdots & \ddots & \vdots \\ g_{I0} & \cdots & g_{1D} \end{bmatrix} \tag{8}$$

where g_{pq} is the weight of between pth neuron of a layer to qth neuron of another layer. In fact, the DNN model has two or more hidden layers. Therefore, the output of the nth layer is as follows:

$$z^{(n)} = AF^{(n)}(a^{(n)}) \tag{9}$$

$$a^{(n)} = G^{(n)} z^{(n-1)} \tag{10}$$

where $AF^{(n)}$ is an appropriate activation function of the nth layer, $G^{(n)}$ is the weight matrix of the nth layer and $z^{(n-1)}$ is the output of previous $(n-1)$ layer. Also, the initial parameter $z^{(0)} = x$ where x is:

$$x = [1, x_1, \dots, x_D]^T \tag{11}$$

which x_j is the jth input variable. Therefore, the network function becomes

$$z^{(n)} = AF^{(n)}(G^{(n)}\left(\dots AF^{(2)}\left(G^{(2)}\left(AF^{(1)}(G^{(1)}x)\right)\right)\dots\right)) \tag{12}$$

The activation function is used to obtain the output of the node. It is also called the transfer function (TF) and is important for constructing a neural network. The activation function can be linear or nonlinear; therefore, in fact, this function determines how the sum of the input nodes is transformed into the output of a node. The popular activation functions include rectified linear activation (ReLU), logistic (sigmoid), hyperbolic tangent (Tanh), linear, etc. It is important to highlight **that** the hyperbolic tangent (tanh) function is defined as

$$AF(x) = \frac{e^x - e^{-x}}{e^x + e^{-x}} \tag{13}$$

where in this case the output of function belongs to $(-1, 1)$ and also, the linear function is expressed as

$$AF(x) = x \tag{14}$$

where in this case the output of function belongs to $(-\infty, \infty)$ and also, the ReLU function is defined as

$$AF(x) = x^+ = \max(0, x) \tag{15}$$

where in this case the output of function belongs to $[0, \infty)$ and also, the logistic function is given by

$$AF(x) = \frac{1}{1+e^{-x}} \tag{16}$$

where in this case the output of function belongs to $(0, 1)$.

AdaBoost

Adaptive Boosting (AdaBoost) is an ensemble learning technique in machine learning, designed for both classification and regression tasks. It operates by initially training a base regressor on the original dataset. Subsequent models are then trained iteratively, with each new regressor placing greater emphasis on the samples that were poorly predicted by the previous ones through weight adjustments. This iterative process allows the algorithm to concentrate on more challenging instances. The AdaBoost algorithm was introduced by (Freund & Schapire, 1997; Drucker, 1997).

Random forest (RF)

The random forest (RF) algorithm is employed for both classification and regression tasks. It is a supervised learning technique that utilizes an ensemble learning approach. The RF algorithm creates a multitude of pending trees during training. Then, the mean or average prediction of the exclusive trees is returned. It is important to highlight that this algorithm is a robust solution for avoiding overfitting. The pseudocode of this algorithm can be expressed as follows:

Random forest (RF) algorithm
1- n samples are randomly selected from the training set.
2- Train a regression tree
3- Once training is complete, predictions for new, unseen samples are generated by aggregating the outputs of all individual regression trees through averaging.
$\hat{y} = \frac{1}{B}\sum_{i=1}^{B} f_i(x_i)$ (17)
where $f_i(x_i)$ is the corresponding output generated by ith the tree and B is the number of a tree.

Model evaluation

Model evaluation is a crucial step in assessing predictive performance and identifying the strengths and limitations of a developed model. It involves the use of quantitative performance metrics to measure the model's accuracy, robustness, and generalization capability. The primary evaluation metrics employed in this study are defined as follows:

$$MSE = \frac{\|\boldsymbol{y}-\hat{\boldsymbol{y}}\|_2^2}{n} \tag{18}$$

where $\boldsymbol{y} = [y_1, y_2, \dots, y_n]^T$ and $\hat{\boldsymbol{y}} = [\hat{y}_1, \hat{y}_2, \dots, \hat{y}_n]^T$. y_i and $\hat{y}_i$ are the measurement value and the predicted value of ith sample. Also, n is the number of samples. The regression coefficient which shows distribution of variables is defined as follows:

$$R^2 = 1 - \frac{\|\boldsymbol{y}-\hat{\boldsymbol{y}}\|_2^2}{\left\|\boldsymbol{y}-\frac{1}{n}\sum_{i=1}^{n} y_i\right\|_2^2} = 1 - \frac{\|\boldsymbol{e}\|_2^2}{\left\|\boldsymbol{y}-\frac{1}{n}\sum_{i=1}^{n} y_i\right\|_2^2} \tag{19}$$

where $\boldsymbol{e}$ is a distance between the measurement and the predicted values. Besides, the equation (19) based on the MSE value can be written as:

$$R^2 = n\left(\frac{1}{n} - \frac{MSE}{\left\|\boldsymbol{y}-\frac{1}{n}\sum_{i=1}^{n} y_i\right\|_2^2}\right) \tag{20}$$

It is important to note that the available dataset is relatively small. Therefore, cross-validation (CV) techniques were employed to obtain a reliable and unbiased estimate of the predictive performance of the developed models. In K-fold cross-validation, the dataset is first randomly shuffled and then partitioned into (K) approximately equal-sized subsets (folds). During each iteration, one fold is used as the testing set, while the remaining $(K-1)$ folds are combined to form the training set. The model is trained using the training data and subsequently evaluated on the corresponding testing fold. This process is repeated (K) times so that each fold serves as the testing set exactly once. For example, $(K = 5)$ was adopted, resulting in five independent training-testing cycles, as illustrated in Fig. 8. For each fold, the prediction error (e.g., MSE) was computed using only the testing samples. The overall performance of the model was then obtained by averaging the errors across all five folds, providing a robust estimate of the model's generalization capability.

$$\text{Avarege MSE} = \frac{1}{5}\sum_{i=1}^{5} MSE_i \tag{21}$$

As the number of folds increases, K-fold cross-validation approaches the Leave-One-Out (LOO) cross-validation scheme. Specifically, LOO can be regarded as a special case of K-fold cross-validation in which the number of folds is equal to the total number of samples. In this approach, a single sample is used as the testing set, while the remaining $(N-1)$ samples are used for training. The procedure is repeated (N) times so that each sample serves as the testing instance exactly once. The overall model performance is then obtained by averaging the prediction errors over all iterations. Since LOO maximizes the amount of training data used in each iteration, it is particularly suitable for small datasets and provides a rigorous assessment of the model's generalization performance.

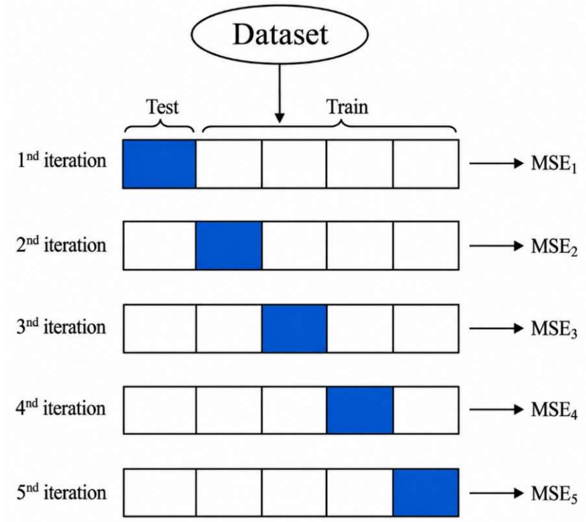

Figure 8. The K-Fold procedure for K=5

Simulation Results

This section evaluates the performance of the mentioned models using performance metrics. A lower MSE and a higher R^2 indicate superior predictive accuracy and better model fitting. The predictive capabilities of the investigated models are systematically compared based on these evaluation criteria. Prior to model implementation and the analysis of prediction results, a sensitivity analysis is conducted to examine the influence of the input variables on the model outputs and to provide a deeper understanding of their relative significance.

Sensitivity analysis

A sensitivity analysis was conducted to quantify the relative contribution of the input variables to the prediction of rock strength. The feature importance scores were obtained using the RF model, where the relative importance of each predictor was computed based on the impurity reduction accumulated over all decision trees in the ensemble. The resulting importance values were normalized so that the sum of all feature importance scores equals one, allowing a direct comparison of the contribution of each input variable. The relative importance scores for the dry and saturated conditions are presented in Fig. 9(a) and Fig. 9(b), respectively. The results indicate that Is_{50}, γ (sat/dry), n and $\mathrm{V_p}$ are the most influential variables for predicting rock strength under both dry and saturated conditions. Among these variables, the wave velocity $\mathrm{V_p}$ exhibits the highest importance score, indicating that it is the dominant predictor of rock strength. This finding is physically consistent, as wave velocity reflects the combined influence of several intrinsic rock characteristics, including porosity, mineral composition, fillings, and petrographic properties, all of which significantly affect the mechanical behavior and strength of the rock. The different predictive performances of the models under dry and saturated conditions can be explained by the influence of water on the mechanical behavior of the Ilam limestone. Under saturated conditions, water penetrates the pore spaces and pre-existing microcracks, reducing interparticle bonding and friction while facilitating crack initiation and propagation. As a result, the relationships between the input parameters and UCS become more complex and nonlinear than those under dry conditions. This complexity is better captured by machine-learning models, particularly RF and DNN, which are capable of modeling nonlinear interactions among the input variables. In contrast, the MR model assumes linear relationships and therefore it has a limited ability to represent the changes in rock behavior caused by saturation. These findings demonstrate that moisture condition is a critical factor affecting both the mechanical properties of limestone and the predictive capability of different modeling approaches. Consequently, machine-learning methods provide a more reliable framework for UCS prediction when moisture-induced variations in rock behavior are significant. Furthermore, the experimental results showed that saturation reduced the average UCS, BTS, and point load index by approximately 32.2%, 31.5%, and 29.9%, respectively. These reductions confirm the significant weakening effect of water on the mechanical behavior of the Ilam limestone and help explain the differences in predictive performance observed under dry and saturated conditions. The complexity and nonlinearity of the mechanical response under saturation further highlight the advantage of machine-learning techniques over conventional regression methods for predicting UCS.

Model performance and comparison

In Table 5, a comparison is made between the simple and multiple linear regressions, which includes four models for the UCS and each of the rock indices, a model containing all the indices, and a model for the UCS and two indices under dry and saturated conditions. For fair comparisons, the same training dataset used previously was used here. Table 5 shows that the UCS model with each of the four indices has less R^2 in UCS prediction for both conditions. Because the four simple models contain only one variable, they cannot achieve high accuracy. However, the UCS model with all the indices has higher performance.

Table 6 shows R^2 and the MSE for each output parameter given by the different models. The better models are the RF and DNN methods for dry and saturated conditions, respectively. Because the RF model yields the lowest MSE and higher R^2 for the saturated condition, the DNN model yields the lowest MSE and higher R^2 for the dry condition with less dispersion. The MSE and R^2 values of the DNN method for the dry condition are equal to 46.06 and 97%, respectively, and the MSE and R^2 values of the RF method for the saturated condition are equal to 46.08 and 96%, respectively.

Table 5. Comparison between simple and multiple linear regression in predicting UCS

Condition	Model	Input data	Equation	R^2
Dry	1	n	UCS = - 22.5383 n + 128.013	0.603
	2	γ_d	UCS = 8.35893 γ_d - 118.678	0.560
	3	V_p	UCS = 0.0068 Vp + 73.830	0.726
	4	Is_{50}	UCS = 10.3187 I_{S50} + 49.186	0.603
	5	γ_d, n	UCS = 4.110 γ_d - 14.997 n + 11.223	0.645
	6	γ_d, Is_{50}	UCS = 6.701 I_{S50} + 4.473 γ_d - 49.897	0.657
	7	n, V_p	UCS = 0.0055Vp - 6.340 n + 86.797	0.739
	8	γ_d, n, V_p , Is_{50}	UCS = 3.089 I_{S50} + 1.407 γ_d - 1.436 n + 0.0047 Vp +32.034	0.910
Sat	1	n	UCS = - 12.551 n + 83.278	0.441
	2	γ_{Sat}	UCS = 5.5323 γ_{Sat} -77.699	0.510
	3	V_p	UCS = 0.0036 Vp + 48.072	0.663
	4	Is_{50}	UCS = 6.914 I_{S50} + 43.730	0.576
	5	γ_{Sat}, n	UCS = - 7.997 n + 4.2296 γ_{Sat} - 33.358	0.590
	6	γ_{Sat}, Is_{50}	UCS = 4.93071 I_{S50} + 2.975 γ_{Sat} -27.4797	0.635
	7	n, V_p	UCS = - 4.4167 n + 0.0031 Vp + 56.353	0.684
	8	γ_{Sat}, n, V_p , Is_{50}	UCS = 2.5361 I_{S50} + 2.010 γ_{Sat} - 1.278 n + 0.0023 Vp - 4.6391	0.90

Table 6. Comparison of predicted result from different models

	MSE		R^2	
	Dry	**Saturation**	**Dry**	**Saturation**
MR	46.45	46.41	91%	90%
DNN	46.06	47.72	97%	74%
RF	46.10	46.08	95%	96%
AdaBoost	47.13	46.93	81%	87%

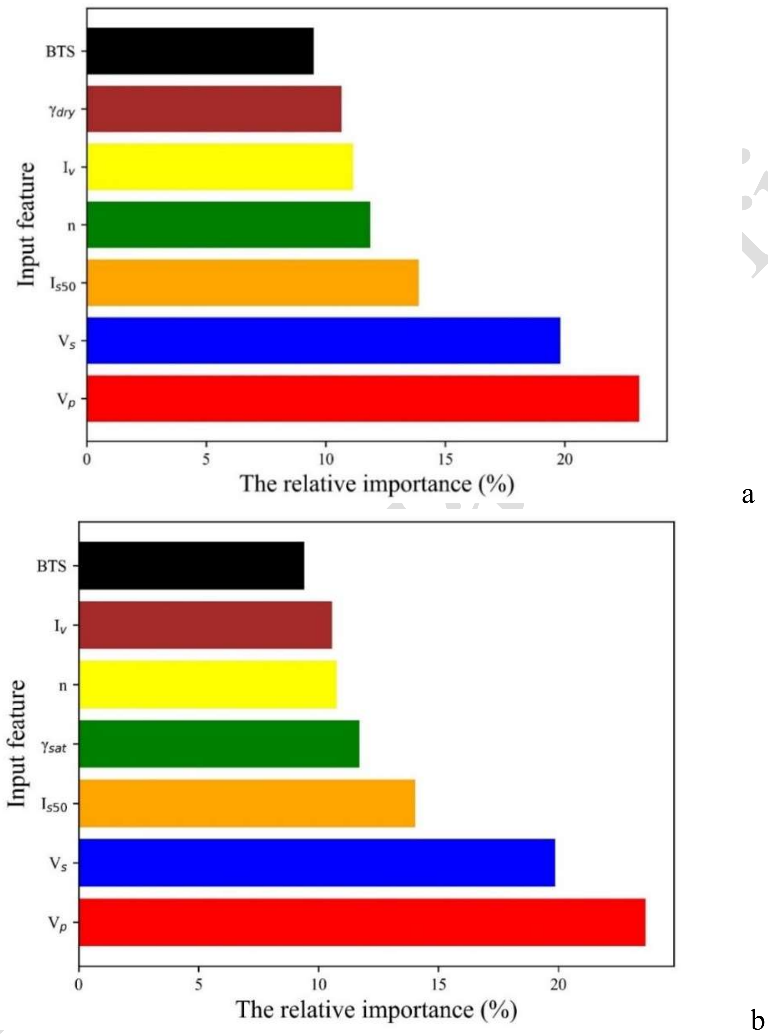

Figure 9. The relative importance of input features a) Dry condition b) Sat condition.

To comprehensively evaluate and compare the performance of the predictive models under both dry and saturated conditions, Taylor diagrams were constructed in Fig.10. These diagrams simultaneously visualize three key statistical measures: the standard deviation (as the radial distance), the correlation coefficient (as the angular component), and the root MSE (RMSE) as contour lines. The reference point (indicated by a star) represents the ideal model with perfect correlation and matching standard deviation. Under dry conditions, the DNN exhibited the highest correlation coefficient (0.97) and a normalized standard deviation closest to the reference, indicating superior agreement with the observed data. RF also showed strong performance with a correlation of 0.95, while MR and AdaBoost performed comparatively lower. In the saturation scenario, RF maintained a high correlation (0.96) and balanced standard deviation, outperforming other models, whereas DNN showed reduced correlation (0.74), suggesting sensitivity to saturation-related variability. Overall, the Taylor diagrams offer a concise yet powerful visualization that highlights DNN's robustness in dry conditions and RF's balanced performance across both scenarios, making them strong candidates for modeling in hydrological or environmental prediction tasks.

Therefore, the DNN model for the dry condition and the RF model for the saturated condition were selected as the most suitable predictive models. The hyperparameters of the selected models, including the number of estimators, maximum tree depth, and other key settings, were determined through an iterative empirical tuning process based on the prediction performance on the validation dataset. The final hyperparameter values adopted for each model are presented in the following section, together with the corresponding prediction results.

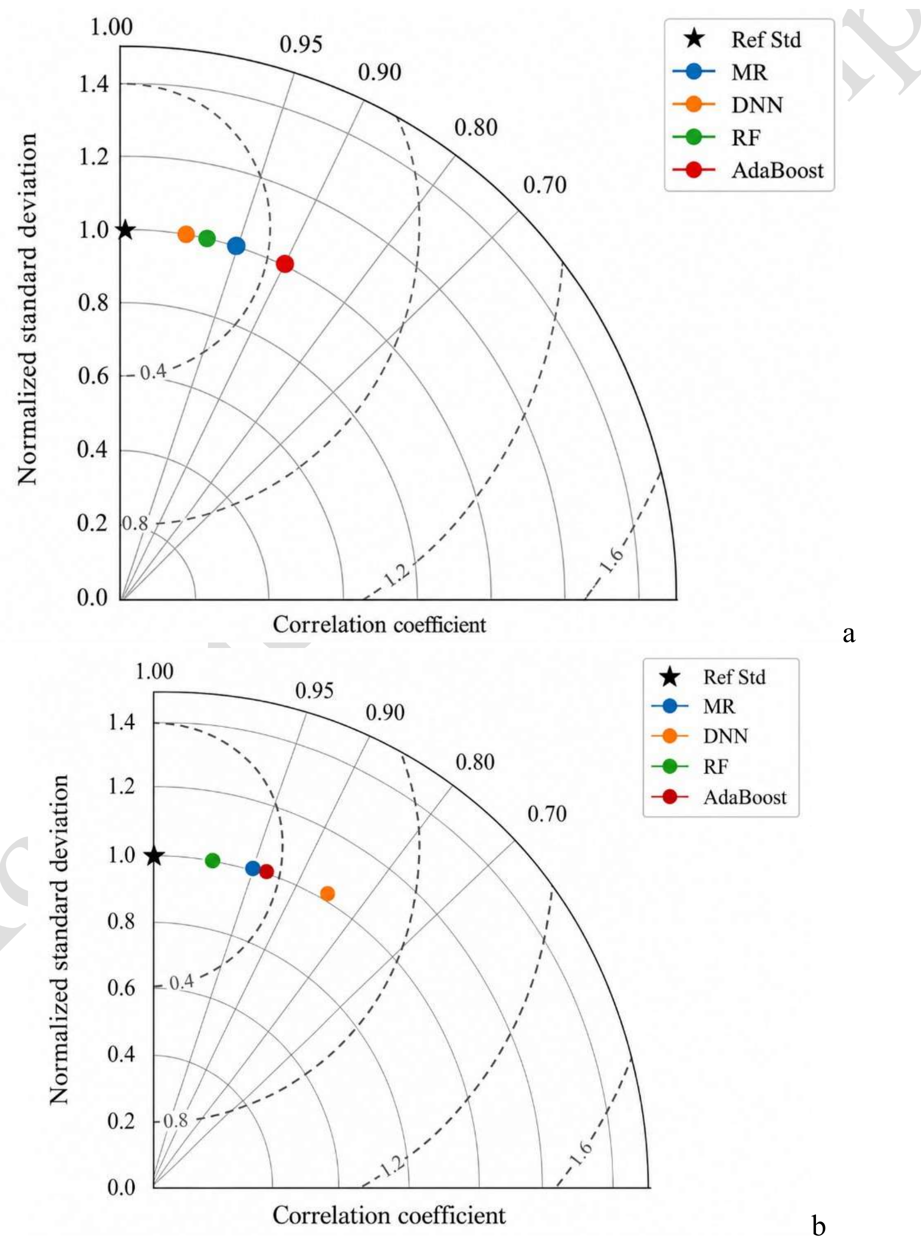

Figure 10. Taylor diagram of the UCS prediction model under (a) Dry condition and (b) Sat condition

Dry condition

Under these conditions, the DNN model demonstrates strong predictive performance. The structure of the proposed DNN is illustrated in Fig. 11, where neurons and biases are represented by blue and red circles, respectively. To determine the optimal hyperparameters, an exhaustive search was conducted across all scenarios and parameter spaces. The most effective hyperparameter configuration identified through this process is summarized in Table 7. The input and hidden layers are interconnected via a weight matrix **G**. During training, the discrepancy between predicted outputs and actual values is used to iteratively update the network's weights. This process continues across all training samples until the specified number of epochs is completed.

Fig. 12 presents the correlation between the measured and predicted UCS values obtained through the K=60 cross-validation for the DNN, MR, RF, and AdaBoost models. The reference line indicates the ideal agreement, providing a visual assessment of the prediction accuracy and consistency of the evaluated models.

Saturated condition

Under saturated conditions, the RF model demonstrated the best predictive performance among the evaluated ML approaches. Fig. 13 illustrates the relationship between the measured and predicted UCS values obtained from the K=60 cross-validation for the RF, DNN, AdaBoost, and MR models. The reference line indicates the ideal agreement between the measured and predicted values, enabling a visual assessment of the prediction accuracy. Furthermore, the RF model achieved the lowest MSE among the evaluated models, confirming its superior predictive accuracy for estimating the UCS under saturated conditions. The performance of the RF model is influenced by several hyperparameters, among which the number of estimators is one of the most important. To determine its optimal value, an empirical tuning procedure was performed by evaluating the MSE for different numbers of estimators.

Table 7. Hyperparameters of the DNN model

DNN model	
The number of hidden layers	2
Batch size	32
Epochs	150
The AF of first hidden layer	Sigmoid
The AF of second hidden layer	Tanh
The AF of output layer	Linear
Optimizer	RMSProp
Loss	MSE

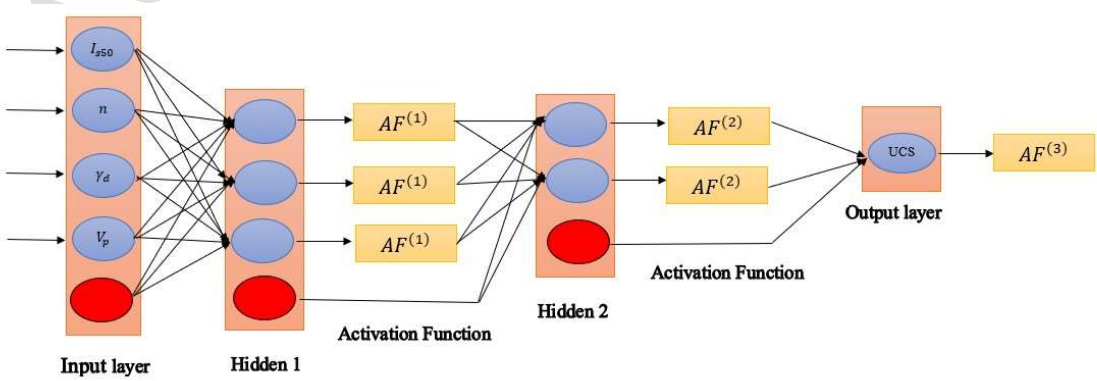

Figure 11. The structure of the DNN

As shown in Fig. 14, the MSE reached its minimum when the number of estimators was set to three. Accordingly, this value was selected as the optimal hyperparameter for the RF model and was adopted in all subsequent analyses.

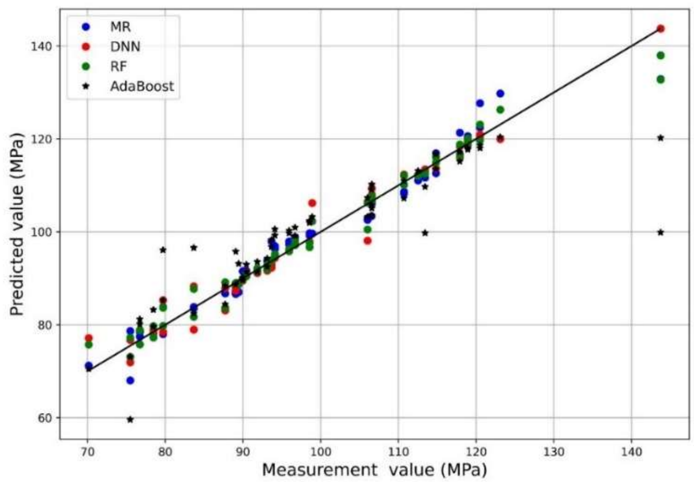

Figure 12. Scatter plot of the predicted versus real values for various methods in dry condition

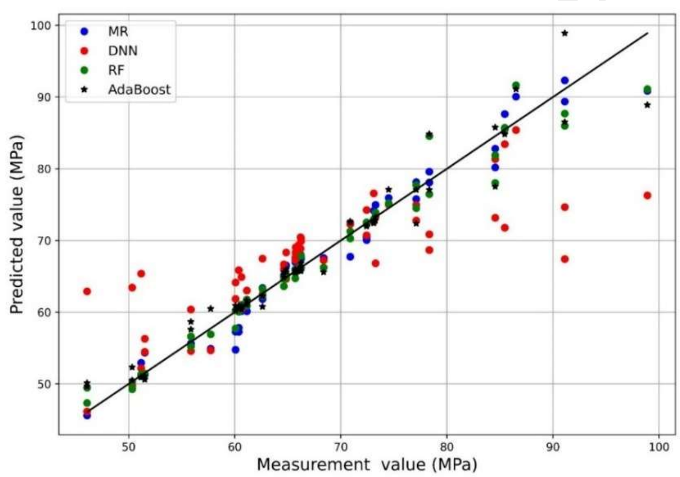

Figure 13. Scatter plot of the predicted versus real values for various methods in saturated condition

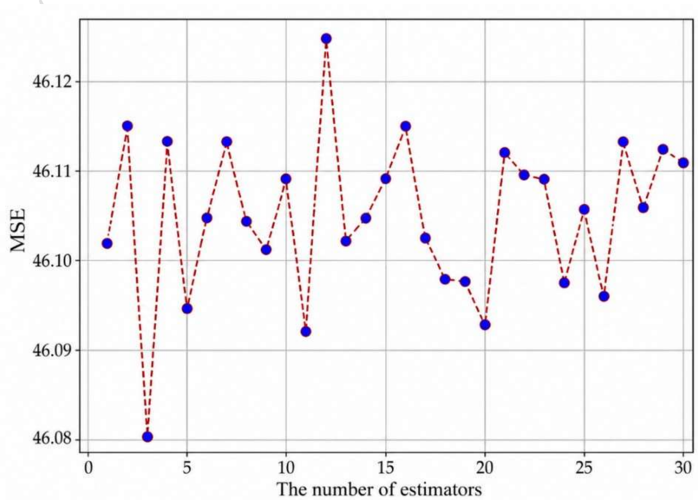

Figure 14. The MSE value versus the number of estimators

The correlation matrix indicates that some input variables are moderately to strongly correlated because they represent involved physical characteristics of the limestone. Some correlations are anticipated their properties such as porosity, density, P-wave velocity, and point load index are all influenced by the rock microstructure and degree of cementation. In the MR model, correlated predictors may introduce multicollinearity, leading to less stable regression coefficients and reducing the interpretability of the model. In contrast, the RF and AdaBoost models are generally less affected by correlated variables because they employ ensemble decision trees and recursive feature selection during model construction. Similarly, the DNN model can effectively capture complex nonlinear relationships among correlated variables. The superior predictive performance of the machine-learning models compared with the MR model suggests that the observed correlations among the input variables did not significantly compromise their predictive capability. However, these correlations should be considered when interpreting the contribution of individual predictors, particularly in the MR model.

Limitations and Future Works

Despite the satisfactory performance of the proposed DNN and RF models, several limitations should be explicitly acknowledged. First, the models are trained and validated using a relatively limited dataset, which may restrict their ability to fully capture the variability of geotechnical properties. Second, the developed models are primarily calibrated for the Ilam Formation limestone under dry and saturated conditions, and their direct applicability to other geological formations or lithological units remains uncertain. Future work will focus on addressing these limitations by expanding the dataset through the inclusion of additional samples from different formations and geological settings. Moreover, independent external validation datasets will be considered to further assess model generalization. The development of more advanced or hybrid machine learning frameworks may also be explored to enhance predictive accuracy and robustness in broader geotechnical applications.

Conclusions

The UCS parameter is necessary for many geotechnical works. Various estimation models have been extended for the determination of UCS indirectly via n, γ, $\mathrm{V_p}$ and $\mathrm{Is_{50}}$ because of the popular use of limestone and the need for UCS parameters. For this purpose, 60 block samples were obtained from the collected limestone blocks. The Ilam limestone formation is grouped into three classes: bioclast wackestone, bioclast wackestone–packstone, and bioclast packstone, and the sedimentary environments are low- and medium-energy. In the present study, four different methods are utilized to predict the UCS. The RF and DNN methods perform best in terms of prediction for dry and saturated conditions, respectively. It is important to highlight that these methods have an acceptable computational cost; therefore, these methods could be the best candidates for predicting the UCS parameter under dry and saturated conditions. The performance of these models depends on the number and quality of samples. The aim of these models was to find suitable equations for the prediction of UCS from easily determinable parameters such as n, γ, $\mathrm{V_p}$ and $\mathrm{Is_{50}}$. In addition, the sensitivity analysis revealed that these parameters have a greater influence on predicting the UCS. Ilam formation is widespread in the oil-rich countries of the Middle East, such as Iran, Iraq, and Saudi Arabia. Therefore, the proposed methods can be used to estimate the UCS of other limestones with similar mineralogies in different places.

Acknowledgements

The authors would like to acknowledge the financial assistance from the Ferdowsi University of Mashhad (FUM), in Iran, which supports the work.

"Appendix"

Appendix A: weight and bias matrices in dry condition.

$$\mathbf{W}_0 = \begin{bmatrix} -0.5838 & 0.824 & 0.2903 \\ 0.3642 & 0.4907 & -0.9847 \\ 0.1394 & -1.1975 & 0.6911 \\ -0.9518 & 0.8231 & 0.5211 \end{bmatrix} \tag{22}$$

$$\mathbf{W}_1 = \begin{bmatrix} 0.637 & -0.6788 \\ 0.7162 & 0.4345 \\ 0.2555 & -0.495 \end{bmatrix} \tag{23}$$

$$\mathbf{W}_2 = \begin{bmatrix} 0.6373 \\ 0.5769 \end{bmatrix} \tag{24}$$

$$\mathbf{b}_0 = \begin{bmatrix} -0.2692 \\ -0.1225 \\ -0.1275 \end{bmatrix} \tag{25}$$

$$\mathbf{b}_1 = \begin{bmatrix} -0.0421 \\ 0.0655 \end{bmatrix} \tag{26}$$

$$\mathbf{b}_2 = [0.0394] \tag{27}$$

Abbreviations

UCS	Uniaxial compressive strength
BTS	Brazilian tensile strength
CV	Cross-validation
RF	Random forest
DNN	Deep neural network
ANN	Artificial neural network
SNN	Simple neural network
AI	**Artificial intelligence**
MR	Multivariate regression
MSE	Mean square error
ML	Machine learning
MLP	Multi-layer perceptron
AF	Activation function
Std. E	Standard error
Std. D	Standard deviation
Max	Maximum
Min	Minimum

List of Symbols

I_v	Water absorption
Is_{50}	Point load index
R^2	coefficient of determination
n	Porosity
V_p	Ultrasonic P-wave velocity
V_s	Ultrasonic S-wave velocity
γ	Unit weight
γ_d	Dry unit weight
γ_{Sat}	Saturation unit weight
$(.)^T$	Transposition sign

$\|.\|_2$	2-norm of a vector
AF(.)	Mapping function from input to activation function
y_i	The measurement value of ith sample
$\hat{y}_i$	The predicted value of ith sample
V_t	The total volume of the specimen
W_d	The dry weight of the specimen
W_{sat}	The saturated weight of the specimen
F	The failure load
A	The area of the cylindrical specimen
D_e	The equivalent core diameter
P	Peak load
W	The smallest specimen width perpendicular to the loading direction
D	The distance between the platens at failure
T	The thickness of the disc
d	The diameter of the disc
t	The pulse travel time
L	The length of specimen

References

Asteris, P. G., Karoglou, M., Skentou, A. D., Vasconcelos, G., He, M., Bakolas, A., Armaghani, D. J., 2024. Predicting uniaxial compressive strength of rocks using ANN models: Incorporating porosity, compressional wave velocity, and Schmidt hammer data. Ultrasonics, 141: 107347.

Amiri, M., Amiri, M., Karrari, S. S., Moradi, S., 2024. Predicting uniaxial compressive strength of different rocks using principal component analysis and deep neural network. Journal of Geomine, 2(2): 78-89.

Abdelhedi, M., Jabbar, R., Said, A. B., Fetais, N., Abbes, C., 2023. Machine learning for prediction of the uniaxial compressive strength within carbonate rocks. Earth Science Informatics, 16(2): 1473-1487.

Al-Husseini, M. I., 2007. Iran's crude oil reserves and production. GeoArabia, 12(2): 69-94.

Alavi, M., 2004. Regional stratigraphy of the Zagros fold-thrust belt of Iran and its proforeland evolution. American journal of Science, 304(1): 1-20.

Anon, O. H., 1979. Classification of rocks and soils for engineering geological mapping. Part 1: rock and soil materials. Bull Int Assoc Eng Geol, 19(1): 364-437.

Armaghani, D. J., Mamou, A., Maraveas, C., Roussis, P. C., Siorikis, V. G., Skentou, A. D., Asteris, P. G., 2021. Predicting the unconfined compressive strength of granite using only two non-destructive test indexes. Geomech. Eng, 25(4): 317-330.

Armaghani, D. J., Tonnizam Mohamad, E., Momeni, E., Monjezi, M., & Sundaram Narayanasamy, M., 2016. Prediction of the strength and elasticity modulus of granite through an expert artificial neural network. Arabian Journal of Geosciences, 9: 1-16.

Armaghani, D. J., Amin, M. F. M., Yagiz, S., Faradonbeh, R. S., & Abdullah, R. A., 2016. Prediction of the uniaxial compressive strength of sandstone using various modeling techniques. International Journal of Rock Mechanics and Mining Sciences, 85: 174-186.

ASTM, D., 2005. 2845-05, Standard method for laboratory determination of pulse velocities and ultrasonic elastic constants of rock. Pennsylvania: ASTM International Standards Worldwide, 1-7.

Broch, E., Franklin, J. A., 1972, November. The point-load strength test. In International Journal of Rock Mechanics and Mining Sciences & Geomechanics Abstracts, 9(6): 669-676, Pergamon.

Barham, W. S., Rabab'ah, S. R., Aldeeky, H. H., Al Hattamleh, O. H., 2020. Mechanical and physical based artificial neural network models for the prediction of the unconfined compressive strength of rock. Geotechnical and geological engineering, 38: 4779-4792.

Çanakcı, H., Baykasoğlu, A., Güllü, H., 2009. Prediction of compressive and tensile strength of Gaziantep basalts via neural networks and gene expression programming. Neural Computing and Applications, 18: 1031-1041.

Cevik, A., Sezer, E. A., Cabalar, A. F., Gokceoglu, C., 2011. Modeling of the uniaxial compressive

strength of some clay-bearing rocks using neural network. Applied Soft Computing, 11(2): 2587-2594.
Drucker, H., 1997, July. Improving regressors using boosting techniques. In Icml, 97: 107-115.
Diamantis, K., Moussas, V. C., 2021. Estimating uniaxial compressive strength of peridotites from simple tests using neural networks. Arabian Journal of Geosciences, 14: 1-13.
Duda, R. O., Hart, P. E., 2006. Pattern classification. John Wiley & Sons.
Dunham, R. J., 1962. Classification of carbonate rocks according to depositional textures.
Fang, Q., Yazdani Bejarbaneh, B., Vatandoust, M., Jahed Armaghani, D., Ramesh Murlidhar, B., Tonnizam Mohamad, E., 2021. Strength evaluation of granite block samples with different predictive models. Engineering with computers, 37: 891-908.
Fausett, L. V., 2006. Fundamentals of neural networks: architectures, algorithms and applications. Pearson Education India.
Fener, M. U. S. T. A. F. A., Kahraman, S. A. İ. R., Bilgil, A., Gunaydin, O., 2005. A comparative evaluation of indirect methods to estimate the compressive strength of rocks. Rock Mechanics and Rock Engineering, 38: 329-343.
Ferentinou, M., Fakir, M., 2017, June. An ANN approach for the prediction of uniaxial compressive strength, of some sedimentary and igneous rocks in eastern KwaZulu-Natal. In ISRM European Rock Mechanics Symposium-EUROCK. OnePetro.
Freund, Y., Schapire, R. E., 1997. A decision-theoretic generalization of on-line learning and an application to boosting. Journal of computer and system sciences, 55(1): 119-139.
Flasiński, M., 2016. Introduction to artificial intelligence. Springer.
Fereidooni, D., Khajevand, R., 2018. Determining the geotechnical characteristics of some sedimentary rocks from Iran with an emphasis on the correlations between physical, index, and mechanical properties. Geotechnical Testing Journal, 41(3): 555-573.
Ghabeishavi, A., Vaziri-Moghaddam, H., Taheri, A., 2009. Facies distribution and sequence stratigraphy of the Coniacian–Santonian succession of the Bangestan Palaeo-high in the Bangestan Anticline, SW Iran. Facies, 55(2): 243-257.
Gokceoglu, C., 2002. A fuzzy triangular chart to predict the uniaxial compressive strength of the Ankara agglomerates from their petrographic composition. Engineering Geology, 66(1-2): 39-51.
Gül, E., Ozdemir, E., Sarıcı, D. E., 2021. Modeling uniaxial compressive strength of some rocks from turkey using soft computing techniques. Measurement, 171, 108781.
Haykin, S. S., Haykin, S. S., 2001. Kalman filtering and neural networks, 284, Wiley Online Library.
Heidari, M., Khanlari, G. R., Torabi Kaveh, M., Kargarian, S., 2012. Predicting the uniaxial compressive and tensile strengths of gypsum rock by point load testing. Rock mechanics and rock engineering, 45: 265-273.
Heydari, E., 2008. Tectonics versus eustatic control on supersequences of the Zagros Mountains of Iran. Tectonophysics, 451(1-4): 56-70.
Hoek, E., Diederichs, M. S., 2006. Empirical estimation of rock mass modulus. International journal of rock mechanics and mining sciences, 43(2): 203-215.
Hollis, C., 2011. Diagenetic controls on reservoir properties of carbonate successions within the Albian–Turonian of the Arabian Plate. Petroleum Geoscience, 17(3): 223-241.
ISRM 2007. The complete ISRM suggested methods for rock characterization, testing, and monitoring: 1974–2006. In: Ulusay, Hudson (eds) Suggested methods prepared by the commission on testing methods. International Society for Rock Mechanics, Compilation Arranged by the ISRM Turkish National Group Ankara, Turkey, p 628.
Jahed Armaghani, D., Safari, V., Fahimifar, A., Mohd Amin, M. F., Monjezi, M., Mohammadi, M. A., 2018. Uniaxial compressive strength prediction through a new technique based on gene expression programming. Neural Computing and Applications, 30: 3523-3532.
Jin, X., Zhao, R., Ma, Y., 2022. Application of a hybrid machine learning model for the prediction of compressive strength and elastic modulus of rocks. Minerals, 12(12): 1506.
Kahraman, S. A. İ. R., 2001. Evaluation of simple methods for assessing the uniaxial compressive strength of rock. International Journal of Rock Mechanics and Mining Sciences, 38(7): 981-994.
Kahraman, S., Gunaydin, O., Alber, M., Fener, M., 2009. Evaluating the strength and deformability properties of Misis fault breccia using artificial neural networks. Expert Systems with Applications, 36(3): 6874-6878.
Kayabasi, A., Gokceoglu, C. A. N. D. A. N., Ercanoglu, M. U. R. A. T., 2003. Estimating the

deformation modulus of rock masses: a comparative study. International Journal of Rock Mechanics and Mining Sciences, 40(1): 55-63.
Kumar, B. R., Vardhan, H., Govindaraj, M., Vijay, G. S., 2013. Regression analysis and ANN models to predict rock properties from sound levels produced during drilling. International Journal of Rock Mechanics and Mining Sciences, 58: 61-72.
Li, D., Armaghani, D. J., Zhou, J., Lai, S. H., Hasanipanah, M., 2020. A GMDH predictive model to predict rock material strength using three non-destructive tests. Journal of Nondestructive Evaluation, 39: 1-14.
Li, J., Li, C., Zhang, S. 2022. Application of Six Metaheuristic Optimization Algorithms and Random Forest in the uniaxial compressive strength of rock prediction. Applied Soft Computing, 131:109729.
Lawal, A. I., Mulenga, F., 2025. Predicting the uniaxial compressive strength of different rock types using implementable stochastically modified artificial neural network and Shapley additive explanations. Multiscale and Multidisciplinary Modeling, Experiments and Design, *8*(10): 469.
Madhubabu, N., Singh, P. K., Kainthola, A., Mahanta, B., Tripathy, A., Singh, T. N., 2016. Prediction of compressive strength and elastic modulus of carbonate rocks. Measurement, *88*: 202-213.
Mehrabi, H., Bagherpour, B., Honarmand, J., 2020. Reservoir quality and micrite textures of microporous intervals in the Upper Cretaceous successions in the Zagros area, SW Iran. Journal of Petroleum Science and Engineering, 192: 107292.
Mehrabi, H., Rahimpour-Bonab, H., Enayati-Bidgoli, A. H., Esrafili-Dizaji, B., 2015. Impact of contrasting paleoclimate on carbonate reservoir architecture: Cases from arid Permo-Triassic and humid Cretaceous platforms in the south and southwestern Iran. Journal of Petroleum Science and Engineering, 126: 262-283.
Mishra, D. A., Basu, A., 2013. Estimation of uniaxial compressive strength of rock materials by index tests using regression analysis and fuzzy inference system. Engineering Geology, 160:54-68.
Mohamad, E. T., Jahed Armaghani, D., Momeni, E., Alavi Nezhad Khalil Abad, S. V., 2015. Prediction of the unconfined compressive strength of soft rocks: a PSO-based ANN approach. Bulletin of Engineering Geology and the Environment, 74: 745-757.
Momeni, E., Armaghani, D. J., Hajihassani, M., Amin, M. F. M., 2015. Prediction of uniaxial compressive strength of rock samples using hybrid particle swarm optimization-based artificial neural networks. Measurement, 60:50-63.
Monjezi, M., Amini Khoshalan, H., Razifard, M., 2012. A neuro-genetic network for predicting uniaxial compressive strength of rocks. Geotechnical and Geological Engineering, 30: 1053-1062.
Motiei, H., 1993. Stratigraphy of Zagros. Geological Survey of Iran Publication.
Moussas, V. C., Diamantis, K., 2021. Predicting uniaxial compressive strength of serpentinites through physical, dynamic and mechanical properties using neural networks. Journal of Rock Mechanics and Geotechnical Engineering, 13(1): 167-175.
Mozumder, R. A., Laskar, A. I., 2015. Prediction of unconfined compressive strength of geopolymer stabilized clayey soil using artificial neural network. Computers and Geotechnics, 69: 291-300.
Navidtalab, A., Sarfi, M., Enayati-Bidgoli, A., Yazdi-Moghadam, M., 2020. Syn-depositional continental rifting of the Southeastern Neo-Tethys margin during the Albian–Cenomanian: evidence from stratigraphic correlation. International Geology Review, 62(13-14): 1698-1723.
Nefeslioglu, H. A., 2013. Evaluation of geo-mechanical properties of very weak and weak rock materials by using non-destructive techniques: Ultrasonic pulse velocity measurements and reflectance spectroscopy. Engineering Geology, 160: 8-20.
Ozbek, A., Unsal, M., Dikec, A., 2013. Estimating uniaxial compressive strength of rocks using genetic expression programming. Journal of Rock Mechanics and Geotechnical Engineering, *5*(4): 325-329.
Ozcelik, Y., Bayram, F., Yasitli, N. E., 2013. Prediction of engineering properties of rocks from microscopic data. Arabian Journal of Geosciences, 6: 3651-3668.
Russell, S. J., 2010. Artificial intelligence a modern approach. Pearson Education, Inc.
Shalabi, F. I., Cording, E. J., Al-Hattamleh, O. H. 2007. Estimation of rock engineering properties using hardness tests. Engineering Geology, 90(3-4), 138-147.
Sharma, L. K., Vishal, V., Singh, T. N., 2017. Developing novel models using neural networks and fuzzy systems for the prediction of strength of rocks from key geomechanical properties. Measurement, 102, 158-169.
Shen, J., Karakus, M., Xu, C., 2012. A comparative study for empirical equations in estimating

deformation modulus of rock masses. Tunnelling and underground space technology, 32: 245-250.
Singh, R., Vishal, V., Singh, T. N., Ranjith, P. G., 2013. A comparative study of generalized regression neural network approach and adaptive neuro-fuzzy inference systems for prediction of unconfined compressive strength of rocks. Neural Computing and Applications, 23: 499-506.
Sonmez, H., Gokceoglu, C., Nefeslioglu, H. A., & Kayabasi, A., 2006. Estimation of rock modulus: for intact rocks with an artificial neural network and for rock masses with a new empirical equation. International Journal of Rock Mechanics and Mining Sciences, 43(2): 224-235.
Setayeshirad, M.R., Uromeie, A, Nikudel, M.R., 2025. Modeling of the Uniaxial Compressive Strength of Carbonate Rocks Using Statistical Analysis and Artificial Neural Network. Rock Mechanics and Rock Engineering, 58:6025–6042.
Tang, L., Na, S., 2021. Comparison of machine learning methods for ground settlement prediction with different tunneling datasets. Journal of Rock Mechanics and Geotechnical Engineering, 13(6):1274-1289.
Teymen, A., Mengüç, E. C., 2020. Comparative evaluation of different statistical tools for the prediction of uniaxial compressive strength of rocks. International Journal of Mining Science and Technology, 30(6): 785-797.
Torabi-Kaveh, M., Naseri, F., Saneie, S., Sarshari, B., 2015. Application of artificial neural networks and multivariate statistics to predict UCS and E using physical properties of Asmari limestones. Arabian journal of Geosciences, 8: 2889-2897.
Wang, M., Wan, W., Zhao, Y., 2020. Prediction of the uniaxial compressive strength of rocks from simple index tests using a random forest predictive model. Comptes Rendus. Mécanique, 348(1): 3-32.
Wang, M., Zhao, G., Liang, W., Wang, N., 2023. A comparative study on the development of hybrid SSA-RF and PSO-RF models for predicting the uniaxial compressive strength of rocks. Case Studies in Construction Materials, 18: e02191.
Willard, R. J., McWilliams, J. R., 1969, January. Microstructural techniques in the study of physical properties of rock. In International Journal of Rock Mechanics and Mining Sciences & Geomechanics Abstracts, 6 (1): 1-12. Pergamon.
Yagiz, S., Sezer, E. A., Gokceoglu, C., 2012. Artificial neural networks and nonlinear regression techniques to assess the influence of slake durability cycles on the prediction of uniaxial compressive strength and modulus of elasticity for carbonate rocks. International Journal for Numerical and Analytical Methods in Geomechanics, 36(14): 1636-1650.
Yesiloglu-Gultekin, N., Gokceoglu, C., 2022 . A comparison among some non-linear prediction tools on indirect determination of uniaxial compressive strength and modulus of elasticity of basalt. Journal of Nondestructive Evaluation, 41(1): 10.
Yesiloglu-Gultekin, N. U. R. G. Ü. L., Gokceoglu, C., Sezer, E. A., 2013. Prediction of uniaxial compressive strength of granitic rocks by various nonlinear tools and comparison of their performances. International Journal of Rock Mechanics and Mining Sciences, 62: 113-122.
Yilmaz, I., Yuksek, G., 2009. Prediction of the strength and elasticity modulus of gypsum using multiple regression, ANN, and ANFIS models. International journal of rock mechanics and mining sciences, 46(4): 803-810.
Yu, Z., Zhou, J., Hu, L., 2023. Prediction of compressive strength of granite: use of machine learning techniques and intelligent system. Earth Science Informatics, 16 (4): 4113-4129.
Zhang, W., Li, H., Li, Y., Liu, H., Chen, Y., Ding, X., 2021. Application of deep learning algorithms in geotechnical engineering: a short critical review. Artificial Intelligence Review, 1-41.
Zhao, T., Song, C., Lu, S., Xu, L., 2022. Prediction of uniaxial compressive strength using fully bayesian gaussian process regression (fB-GPR) with model class selection. Rock Mechanics and Rock Engineering, 55(10): 6301-6319.
Zhao, R., Shi, S., Li, S., Guo, W., Zhang, T., Li, X., Lu, J., 2023. Deep learning for intelligent prediction of rock strength by adopting measurement while drilling data. International Journal of Geomechanics, 23(4): 04023028.
Zorlu, K., Gokceoglu, C., Ocakoglu, F., Nefeslioglu, H. A., Acikalin, S. J. E. G., 2008. Prediction of uniaxial compressive strength of sandstones using petrography-based models. Engineering Geology, 96(3-4): 141-158.